View metadata, citation and similar papers at core.ac.uk
brought to you by CORE
provided by Caltech Authors - Main

ACS APPLIED MATERIALS & INTERFACES

Caltech Library

Subscriber access provided by Caltech Library

Surfaces, Interfaces, and Applications

Genesis and Propagation of Fractal Structures During Photoelectrochemical Etching of n-Silicon

Matthias H. Richter, Michael Lublow, Kimberly M. Papadantonakis, Nathan S. Lewis, and Hans-Joachim Lewerenz

ACS Appl. Mater. Interfaces, **Just Accepted Manuscript** • DOI: 10.1021/acsami.9b22900 • Publication Date (Web): 16 Mar 2020

Downloaded from pubs.acs.org on March 17, 2020

Just Accepted

"Just Accepted" manuscripts have been peer-reviewed and accepted for publication. They are posted online prior to technical editing, formatting for publication and author proofing. The American Chemical Society provides "Just Accepted" as a service to the research community to expedite the dissemination of scientific material as soon as possible after acceptance. "Just Accepted" manuscripts appear in full in PDF format accompanied by an HTML abstract. "Just Accepted" manuscripts have been fully peer reviewed, but should not be considered the official version of record. They are citable by the Digital Object Identifier (DOI®). "Just Accepted" is an optional service offered to authors. Therefore, the "Just Accepted" Web site may not include all articles that will be published in the journal. After a manuscript is technically edited and formatted, it will be removed from the "Just Accepted" Web site and published as an ASAP article. Note that technical editing may introduce minor changes to the manuscript text and/or graphics which could affect content, and all legal disclaimers and ethical guidelines that apply to the journal pertain. ACS cannot be held responsible for errors or consequences arising from the use of information contained in these "Just Accepted" manuscripts.

is published by the American Chemical Society. 1155 Sixteenth Street N.W., Washington, DC 20036
Published by American Chemical Society. Copyright © American Chemical Society. However, no copyright claim is made to original U.S. Government works, or works produced by employees of any Commonwealth realm Crown government in the course of their duties.

1
2
3
4
5
6
7
8
9
10
11
12
13
14
15
16
17
18
19
20
21
22
23
24
25
26
27
28
29
30
31
32
33
34
35
36
37
38
39
40
41
42
43
44
45
46
47
48
49
50
51
52
53
54
55
56
57
58
59
60

Genesis and Propagation of Fractal Structures During Photoelectrochemical Etching of n-Silicon

Matthias H. Richter[1], Michael Lublow[2‡*], Kimberly M. Papadantonakis[1],
Nathan S. Lewis[1*], Hans-Joachim Lewerenz[3,4]

1 Division of Chemistry and Chemical Engineering, California Institute of Technology, Pasadena, CA 91125, USA.

2 Technische Universität Berlin, Institut für Chemie, Straße des 17. Juni 124, 10623 Berlin, Germany.

3 Division of Engineering and Applied Science, California Institute of Technology, Pasadena, CA 91125, USA.

4 Technische Universität Berlin, Institut für Festkörperphysik, Hardenbergstrasse 36, 10623, Berlin, Germany.

*Correspondence to: Michael.Lublow@vdivde-it.de; nslewis@caltech.edu

‡Current Address: VDI/VDE Innovation + Technik GmbH, Steinplatz 1, 10623 Berlin, Germany

KEYWORDS

Fractal structures, Silicon, Photoelectrochemistry, Photoelectron spectroscopy

1
2
3
4
5
6
7
8
9
10
11
12
13
14
15
16
17
18
19
20
21
22
23
24
25
26
27
28
29
30
31
32
33
34
35
36
37
38
39
40
41
42
43
44
45
46
47
48
49
50
51
52
53
54
55
56
57
58
59
60

Abstract

The genesis, propagation, and dimensions of fractal-etch patterns that form anodically on front- or back-illuminated n-Si(100) photoelectrodes in contact with 11.9 M NH_4F(aq) has been investigated during either linear-sweep voltammetry or when the electrode was held at a constant potential (E = +6.0 V versus Ag/AgCl). Optical images collected in situ during electrochemical experiments revealed the location and underlying mechanism of initiation and propagation of the structures on the surface. X-ray photoelectron spectroscopic (XPS) data collected for samples emersed from the electrolyte at varied times provided detailed information about the chemistry of the surface during fractal etching. The fractal structure was strongly influenced by the orientation of the crystalline Si sample. The etch patterns were initially generated at points along the circumference of bubbles that formed upon immersion of n-Si(100) samples in the electrolyte, most likely due to the electrochemical and electronic isolation of areas beneath bubbles. XPS data showed the presence of a tensile-stressed silicon surface throughout the etching process as well as the presence of SiO_xF_y on the surface. The two-dimensional fractal dimension $D_{f,2D}$ of the patterns increased with etching time to a maximum observed value of $D_{f,2D}$=1.82. Promotion of fractal etching near etch masks that electrochemically and electronically isolated areas of the photoelectrode surface enabled the selective placement of highly branched structures at desired locations on an electrode surface.

1
2
3
4
5
6
7
8
9
10
11
12
13
14
15
16
17
18
19
20
21
22
23
24
25
26
27
28
29
30
31
32
33
34
35
36
37
38
39
40
41
42
43
44
45
46
47
48
49
50
51
52
53
54
55
56
57
58
59
60

Introduction

Spontaneous structuring is a nonequilibrium process that is often observed in systems having local interactions involving nonlinear dynamics, such as positive- or negative-feedback mechanisms. For example, in physiology, the evolution of hierarchical branching networks, such as found in circulatory and respiratory systems, has been attributed to nonlinear relationships between exchange-surface areas, transport times, and distances. [1] [2] Nonlinear relationships between electrochemically or photoelectrochemically active surface areas, charge transport, and charge-carrier generation can also produce localized structures. The factors contributing to structuring in photoelectrochemistry include electrode kinetics, illumination levels, absorption and diffusion profiles, mass transport in the electrolyte, and the electrode potential. [3] [4] [5]

The formation of porous silicon during the anodic electropolishing of Si in aqueous hydrofluoric acid provides a prominent example of controlled structuring in electrochemistry. [6] [7] Anodic etching of Si photoelectrodes in fluoride-containing electrolytes involves competition between oxide formation and dissolution and different concentrations and electrolytes are expected to yield different behavior. It can result in a range of surface structures, including atomically smooth surfaces, trenches, [8] and uniformly porous surfaces. [9] Theoretical and descriptive models for the electrolytic shaping of oxides have been developed, [10] [11] and electrodes with fractal-like surface trenches have been realized experimentally. [12] [13] [14] [15]

Structured branched systems can be numerically described by their fractal dimension. Each section of a branched structure in which each subsection has new branches at its end resembles the branched structure itself, e.g. a tree. For perfectly symmetrical structures, each part is a perfect replica of the whole structure. Due physical limitations in nature, a structure does not need to be perfectly self-similar to be described by a fractal and its fractal dimension.

Si is an attractive material for the study of complex photoelectrochemical phenomena such as controlled structuring and fractal cracking [16] because the (photo)electrochemistry, surface chemistry, and interface behavior of Si have been studied extensively due to the technological importance of silicon and its oxide. [17] [18] [19] [20] [21] [22] [23] [24] The cracking behavior of Si is of particular interest to battery research, with Si regarded as one of the most promising anode materials for next-generation lithium-ion batteries but cracking is observed upon repeated intercalation and deintercalation of Li. [25]

Synthetic methods that produce microstructured materials with maximized electrochemical surface areas and minimized charge-carrier transport distances and resistances would be of interest for a variety of applications, including electrocatalysis, photocatalysis, [26] energy storage, [27] energy conversion, [28] [29] sensing, and photonics. The challenge inherent to exploitation of regular microstructures is associated with the need to exert control over aspects of the process, such as the location, orientation, or uniformity of the structures. For example, placement of branched structures exclusively near electrocatalysts on an electrode surface could improve the selectivity of the surface for the desired reaction by favoring charge transport to the catalyst relative to transport to other locations where undesired reactions (such as corrosion or other competing surface reactions) may occur.

Herein, we investigated the origin and propagation of fractal-etch patterns that are observed to be formed on illuminated n-Si(100) surfaces during anodic etching in NH_4F(aq). Ammonium fluoride is a strong electrolyte and therefore almost completely dissociates into fluoride and ammonium ions. The fluoride can react further with water and hydronium ions to form HF, HF_2^-. The etching rate is essential independent on the F^- concentration but is strongly dependent on the concentration of HF and HF_2^-. [30] Electrochemical data, optical images of the patterns collected in situ during fractal etching, and X-ray photoelectron spectroscopic (XPS) data were obtained to characterize the chemistry of the surface as the fractal etching progressed.

Experimental section

Materials

Czochralski-grown n-type Si(100) wafers (Addison Engineering, Inc.) and n-type Si(111) wafers (Siltronix) with resistances of 5–25 Ω·cm and a thickness of 505-545 μm were cleaned with ethanol, rinsed with deionized water (18.2 MΩ·cm) and dried with N_2(g). The Si wafers were etched in Buffer HF (a 6:1 (v:v) mixture of NH_4F and HF, obtained from Transene, Inc.) for 30 s, rinsed in deionized water, and dried with N_2(g). For the back contact a drop of In/Ga eutectic was scratched into the back of the electrodes using a carbide scribe. The eutectic was only applied to the edges and thus leaving the center exposed to allow for back illumination.

1
2
3
4
5
6
7
8
9
10
11
12
13
14
15
16
17
18
19
20
21
22
23
24
25
26
27
28
29
30
31
32
33
34
35
36
37
38
39
40
41
42
43
44
45
46
47
48
49
50
51
52
53
54
55
56
57
58
59
60

Electrochemistry

Electrochemistry was performed using a single-compartment polytetrafluoroethylene (PTFE) electrochemical cell (Figure S1) designed to allow for illumination of either the back or front of the Si wafer. The cell was equipped with quartz windows and a saturated KCl Ag/AgCl reference electrode (CH Instruments). A Pt wire was used as the counter electrode. The electrodes were connected to a Biologic SP-200 potentiostat, and the electrolyte was 11.9 M (40 %) ammonium fluoride (NH_4F, Semiconductor grade obtained from Sigma Aldrich, pH = 7.2). Concentrated NH_4F(aq) was prepared by adding NH_4F salt (Sigma Aldrich, ACS reagent grade) to 11.9 M NH_4F(aq) solution. All samples were positioned vertically, and the sample area was 0.5 cm^2 (circle diameter of 8 mm). Illumination was produced by a tungsten-iodide (W-I) lamp calibrated to provide light intensities of ~ 0.2 $mW \cdot cm^{-2}$ to ~ 50 $mW \cdot cm^{-2}$. A high-power 455 nm (2.7 eV) light-emitting diode (LED) with a total focused intensity of 10 mW was used for monochromatic illumination above the band gap of Si. Linear-sweep voltammetry was performed at a scan rate of 10 $mV \cdot s^{-1}$.

X-ray photoelectron spectroscopy

XPS was performed using a Kratos Axis Ultra system with a base pressure of ~ 10^{-10} mbar. The monochromatic Al Kα (hν=1489.6 eV) source had a power of 150 W. High-resolution scans were taken using a pass energy of 5 eV. The photoelectron take-off angle was 0 ° with respect to the surface normal. Samples were removed from the electrolyte under applied potential (emersion); rinsed; dried under a stream of N_2(g); placed into a N_2(g)-flushed XPS-transfer box; and transferred directly to the XPS system. The samples were grounded through their ohmic back contacts. Charge neutralization was not used because for SiO_2 thicknesses up to a few nm the wet, fluoride-containing silicon dioxide produced in these experiments did not result in an observable shift of the XPS binding energies. Based on the resistivity of the Si and the 98.74 eV difference in energy between the intrinsic Si $2p^{3/2}$ peak and valence-band maximum, a Si $2p^{3/2}$ binding energy of ~ 99.55 eV is predicted. [31] The average Si $2p^{3/2}$ binding energy observed in this study was 99.57±0.1 eV, in excellent accord with the theoretically predicted binding energy.

Optical imaging

A Nikon ECLIPSE LV100 digital microscope equipped with a Nikon DS-Fi1 camera was used to image the samples ex-situ after experiments. In-situ imaging was performed using an AXIS network camera during back illumination of the sample.

1
2
3
4
5
6
7
8
9
10
11
12
13
14
15
16
17
18
19
20
21
22
23
24
25
26
27
28
29
30
31
32
33
34
35
36
37
38
39
40
41
42
43
44
45
46
47
48
49
50
51
52
53
54
55
56
57
58
59
60

Calculation of fractal dimensions

The two-dimensional fractal dimension ($D_{f,2D}$, Hausdorff dimension) was calculated from black-and-white micrographs of structures, using a numerical method that relied on counting the number of boxes with window size ε that were required to fully cover the fractals (with each box containing at least one black pixel). The window size, ε, was successively increased from one pixel to the full image size, yielding a plot of the required number of boxes, $\log(N(\varepsilon))$ versus $\log(1/\varepsilon)$. The resulting data were fitted using a line with the functional form $\log(N(\varepsilon)) = D_{f,2D}\cdot\log(1/\varepsilon)+c$, where the parameter c accounted for the non-ideal representation of the structures by an imperfect image with restricted resolution. Typically, for non-fractal two-dimensional images, such as filled circles or squares, $D_{f,2D} = 2$, while for smooth lines $D_{f,2D} = 1$. The calculation was tested against two example patterns such as the Koch curve [32] and the Sierpinski triangle, [32] and produced values of $D_{f,2D}$ that were in close agreement with documented values (Figure S2). The analytically known values for $D_{f,2D}$, in these two systems provided verification of the numerical approach used to determine $D_{f,2D}$, but they were not used to simulate the experimental results.

Results and Discussion

Initiation of fractal etching

Figure 1a shows the current-density versus potential (*J-E*) behavior for front- or back-illuminated n-Si(100) samples in contact with 11.9 M NH_4F(aq) during a linear potential sweep. The light intensity was 10 mW·cm^{-2} for front-illuminated samples (F), and was 50 mW·cm^{-2} for back-illuminated samples (B). As the potential, E, was increased positively from the open-circuit potential, E_{oc}, a peak in current density was observed at $E \sim -0.5$ V (vs. Ag/AgCl); this peak was followed by a passive, low-current-density region until an increase in current density was observed at $E \sim +1.2$ V. For both front- and back-illuminated samples, a second peak was observed at $E \sim +3.5$ V and this peak was followed by a steep increase in current density until a plateau was observed at $E > +6$ V. This *J-E* behavior is qualitatively similar to that of illuminated n-Si(100) in 2.5 % HF(aq). [33]

Figure 1b-g shows optical images collected in situ during a potential scan from E_{oc} to $E = +6$ V, for a sample illuminated from the back. The appearance of structures on the sample surface coincided with the increase in current density observed near $E = +2$ V as well as with visual observation of bubble formation. At the potential where the current density increased, branched

structures (fractals) were not observed. At $E > +2$ V, gas evolution produced small (< 50 µm) transparent bubbles over the entire substrate (Figure 1c). The formation of fractal structures began at potentials between $E = +3$ V and $E = +4$ V, where a local maximum and a kink were present in the J-E characteristic for both front- and back-side-illuminated samples. In addition to the gas evolution observed at $E > +2$ V, larger (> 100 µm) white bubbles were observed at the more positive potentials at which fractal formation prevailed (Figure 1d-g, bubbles marked by arrows). The larger white bubbles were only observed near the tips of the fractals, where silicon was being laterally etched to produce the fractal-etch pattern. A video captured during the potential sweep is included as supporting information.

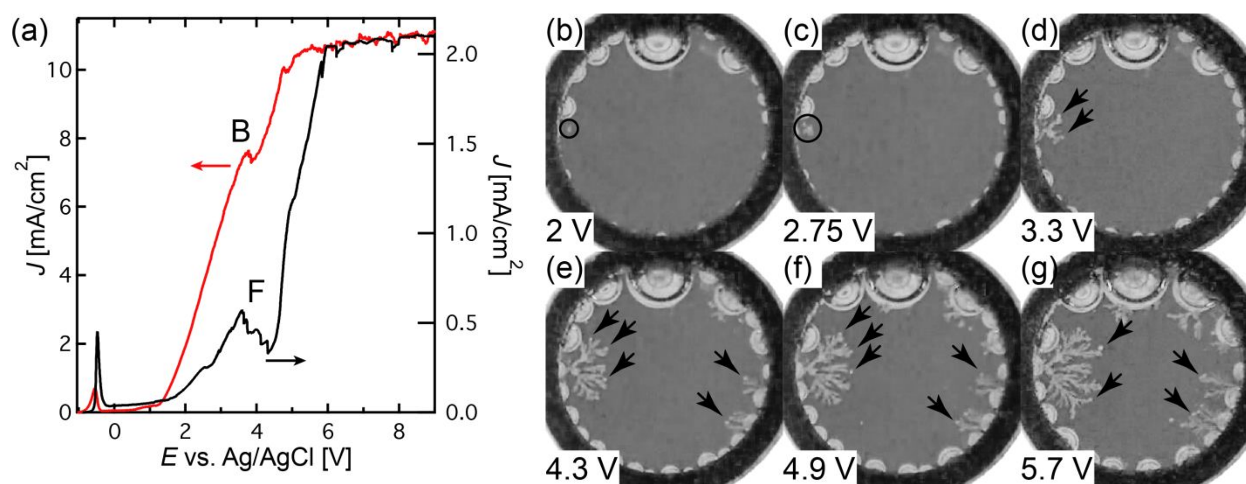

Figure 1: (a) Current density vs. potential scans for illuminated n-Si(100) samples in contact with 11.9 M NH_4F(aq), starting at the open-circuit potential ($E = -0.8$ V) with a scan rate of 10 mV·s^{-1}. Illumination intensities were 50 mW·cm^{-2} for back-illuminated samples (B, left axis), and 10 mW·cm^{-2} for front-illuminated samples (F, right axis). (b-g) In-situ optical images collected during a potential scan for a back-illuminated sample: (b) first etch pattern formed at $E = +2$ V (black circle); (c) $E = +2.75$ V (star-shaped etch structure); (d), (e), (f), (g) as indicated. Evolution of a white-appearing gas via ~ 100 µm diameter bubbles was observed at the very tips of the fractals (locations indicated by arrows).

Figure 2 shows XPS data in the regions of the core-level signals for Si 2p, O 1s and F 1s, respectively, for back-illuminated samples removed from the electrolyte at varied potentials during a potential sweep. For potentials $E < +2.75$ V, signals indicative of a surface oxide with a thickness

1 2 3 4 5 6 7 8 9 10 11 12 13 14 15 16 17 18 19 20 21 22 23 24 25 26 27 28 29 30 31 32 33 34 35 36 37 38 39 40 41 42 43 44 45 46 47 48 49 50 51 52 53 54 55 56 57 58 59 60

of ~ 0.2 nm were observed in the Si 2p and O 1s spectra, and fluorine was not detected. For samples removed under applied potentials of E = +2.75 V or E = +4.5 V, an increase in the intensity of the Si^{4+} 2p core-level-photoemission line, characteristic of SiO_2, and intense O 1s and F 1s photoemission lines, were observed, in conjunction with an oxide thickness of ~ 2.3 nm. Furthermore, the Si^{4+} 2p and O 1s core levels appeared at higher binding energies (533.7 eV for O 1s and 104.6 eV for Si^{4+} 2p) than the commonly observed values for SiO_2 (533.0 eV for O 1s and 103.4 eV for Si^{4+} 2p). Inspection of the binding energies of the O 1s and Si^{4+} 2p core-level-photoemission lines indicated that SiO_2, surface OH groups and H_2O were present for $E = E_{oc}$ to E = +1.0 V. At E = +2.75 V and E = +4.5 V, SiO_xF_y was present on the surface, [34] and at E = +6 V, no SiO_2 was observed and only surface-bound OH and H_2O were detected. Oxygen, silicon, fluorine core levels could be split into different chemical contributions (peak assignments are discussed in more detail later).

Figure S3 shows in more detail the evolution of the peak intensities and chemical state when the linear sweep was terminated at various potentials. It is observed that the evolution of the different silicon, oxygen and fluorine species coincides with the appearance of fractal etching structures. Their intensity the decreases again with prolonged etching and surface coverage of fractals. Primarily it can be observed that the SiO_xF_y species only appear at potential at which fractal etching is observed (E > +2.75 V), whereas hydroxide and SiO_2 are also observed in addition between E_{OC} and 0 V corresponding to the first anodic current peak and oxidation of silicon.

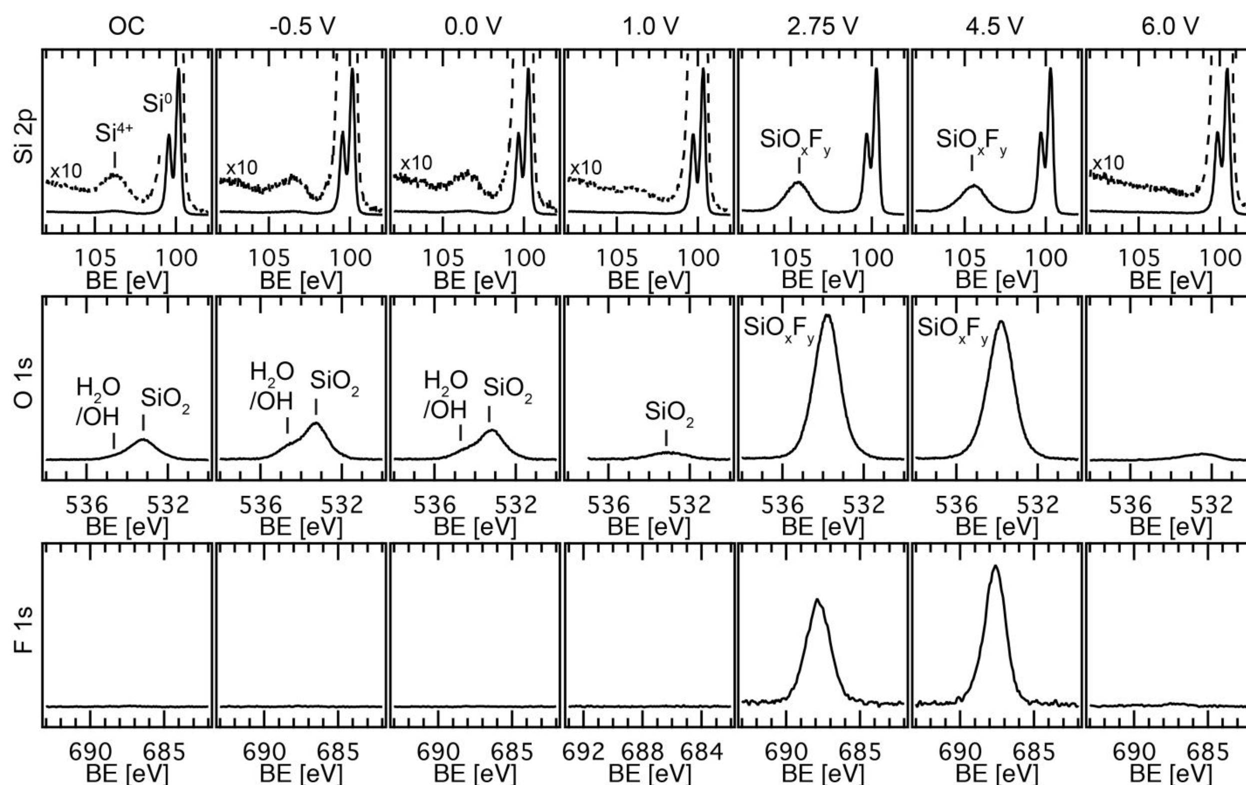

Figure 2: X-ray photoelectron core-level spectra in the Si 2p, O 1s, and F 1s regions for an n-Si(100) sample after emersion at the indicated potentials from a potential sweep in contact with 11.9 M NH_4F(aq). Intensities have been normalized with respect to the intensity of the Si^0 core-level-photoemission line. For the Si 2p core levels a x10 magnified spectra (dashed) line is included to assess the presence of SiO_2.

Pattern development and propagation

Figure 3a shows chronoamperograms (CAs) for n-Si(100) samples under various illumination intensities while in contact with 11.9 M NH_4F(aq) and held for 10 min (up to 20 min for 50 mW·cm^{-2} back illumination) at E = +6.0 V. In addition to the CA obtained without illumination (J = 0 mW·cm^{-2}), two CAs are shown for front illumination (J = 10 mW·cm^{-2} and 20 mW·cm^{-2}, respectively), and a CA is shown for a back-illuminated sample (50 mW·cm^{-2}). Although a higher intensity was used for back illumination to adjust for absorption by the electrolyte and for the diffusion profiles of the excess minority carriers, the photocurrent from the ~ 0.5 mm thick wafer scaled proportionally with the light intensity, consistent with large minority-carrier (hole) diffusion lengths. After an initial current spike, the CAs of the samples showed an

1
2
3
4
5
6
7
8
9
10
11
12
13
14
15
16
17
18
19
20
21
22
23
24
25
26
27
28
29
30
31
32
33
34
35
36
37
38
39
40
41
42
43
44
45
46
47
48
49
50
51
52
53
54
55
56
57
58
59
60

asymptotic current behavior in which the current increased over time. This effect was more pronounced for increased light intensities.

Figures 3b-f show optical micrographs of fractal patterns formed on n-Si(100) during chronoamperometric conditions at E = +6.0 V while under back-side illumination of 50 $mW \cdot cm^{-2}$. The samples were removed from the electrolyte at varied times (1–20 min) while under potential control. In the initial 5 min, a circular etch pattern formed in a location where a bubble had formed upon immersion of the sample in the electrolyte (Figure 3b, c). At the center spot of the initial bubble a cross pattern is visible in Figure 3c which has its origin from Si(110) planes, and is thus also aligned with the subsequently visible boundary box to which the pattern is confined. The cross itself was only visible in the first minutes and is not observed at later stages of etching. The propagation of the etch pattern at the outside of the initial bubble is rotated 45° to it as indicated by arrows. After 5 min, square etch patterns with the two-fold azimuthal symmetry of n-Si(100) were observed (Figure 3d). [13] After 10 min it is visible that the propagation of the etch pattern is confined within the limits of a square of Si(110) lattice planes (Figure 3e). The size of the square and the etch pattern increases with time (Figure 3f). The square can be more clearly seen in Figure S5.

The observed shape resembles the lattice symmetry of the underlying Si(100) substrate with the direction of development of the structure being consistent with the general orientation of the lattice planes (Figure 3g). During formation of the square etch pattern, the boundaries were aligned with Si(110) lattice planes (Figure 3f) which have higher surface energy and etch rate than Si(100), [35] and the parent branches of the fractal pattern propagated along a direction of 45° to it following the <100> direction. [15] The depths of the fractal structures on a back-illuminated sample after 10 min were between 0.7 and 3 μm (Figure S4).

After prolonged etching (20 min, Figure 3f), the etch pattern had propagated into the circular area that had been covered by the initial gas bubble. The differences in the widths and lengths of the features inside and outside of the circular area, respectively, indicate that etch features inside the circular area formed after the initial gas bubble detached from the surface. Similarly, etch patterns that developed adjacent to an initially present gas bubble on a front-side illuminated sample did not extend into the circular area (Figure S5), and no substantial difference was observed between the fractal etch patterns formed on front-illuminated and back-illuminated samples. No evidence of complex bubble geometry, such as superimposed bubbles, was observed.

A control experiment under vigorous stirring of the electrolyte was performed for fractal pattern formation on n-Si(100) at E = +6.0 V under back-side illumination of 50 mW·cm^{-2} for two different durations, to investigate the influence of forced electrolyte convection on the propagation of fractals. Figure S6a shows the chronoamperograms for 10 and 20 min, respectively, of total etching time. Compared to the optical images of resulting fractals without stirring (Figure 3e, f), forced convection resulted in a deformation in the circumference of the initial bubble but fractal growth was still observed (Figure S6b, c).

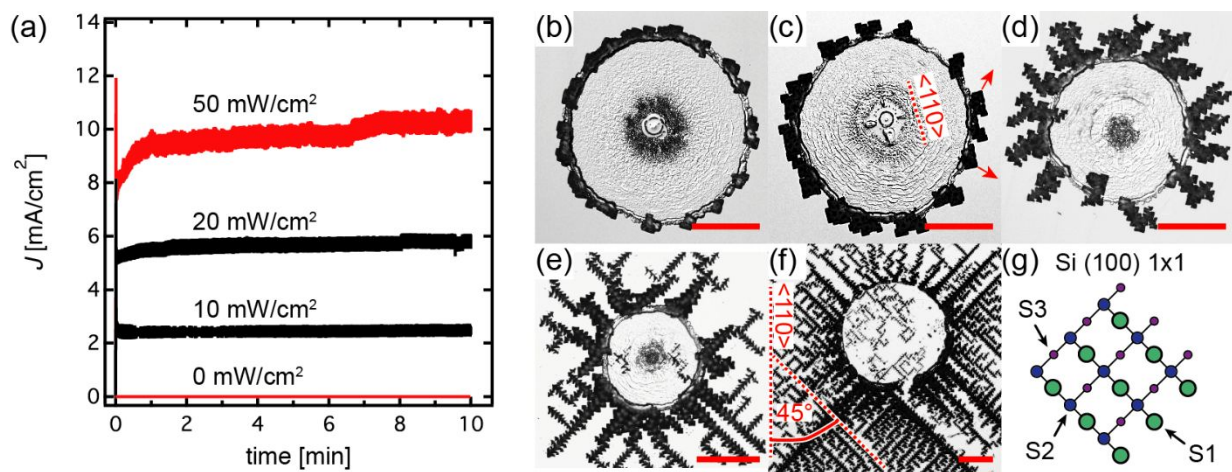

Figure 3: (a) Chronoamperometric profiles at E = +6.0 V vs. Ag/AgCl in 11.9 M NH_4F(aq) for front illumination (black lines, 10 and 20 mW·cm^{-2}), back illumination (red line, 50 mW·cm^{-2}) and in the dark (bottom red line). (b-f) Representative optical images of fractals on n-Si(100) samples when chronoamperometry at E = +6.0 V under 50 mW·cm^{-2} white-light back illumination was stopped at different times: (b) 1 min, (c) 2 min, (d) 5 min, (e) 10 min, (f) 20 min. The trace of the initial gas bubble is visible in the center of the fractal pattern. Each scale bar has a size of 100 μm. (g) The corresponding lattice (top view) of a Si(100) surface; the top layer of Si atoms is indicated by the circular symbols labeled S1, the second layer by S2, and the third layer by S3.

Figure 4 shows O 1s, Si 2p, and F 1s XPS data collected for samples that were removed from the electrolyte under potential control and directly transferred to the analysis chamber, after various durations of CA at E = +6.0 V. The XPS data were collected before the optical micrographs (Figure 3 b-f). The Si 2p line (Figure 4b) showed the formation of oxidized silicon

species in the early stage (t = 1 min, as evidenced by the presence of peak at a binding energy of 104.6 eV (Si^{4+}). For increased etching times, the intensity of the Si^{4+} core-level emission signal decreased substantially, and shifted to lower binding energies, as also observed in the XPS results for the *J-E* scan from E = +2.75 V to E = +6.0 V (Figure 2). Closer inspection of the Si 2p core-level spectra at high gain (5x) revealed small amounts of Si^{4+} and Si^{3+}, which were more visible in the corresponding spectra of CA-treated surfaces (Figure 4b, 20 min).

The O 1s spectra (Figure 4c) showed that the intensity of the O 1s core level, which was attributed to silicon oxide, was reduced after prolonged etching times, with only a small peak at a binding energy of 533 eV remaining after 10 min of CA attributable to SiO_xF_y species. The change in binding energy for O 1s, F 1s, and Si^{4+} 2p indicated the presence of various different surface species (SiO_2, OH groups, and SiO_xF_y species) whose amounts changed over time, e.g. decrease in intensity for prolonged etching time and fractal surface coverage.

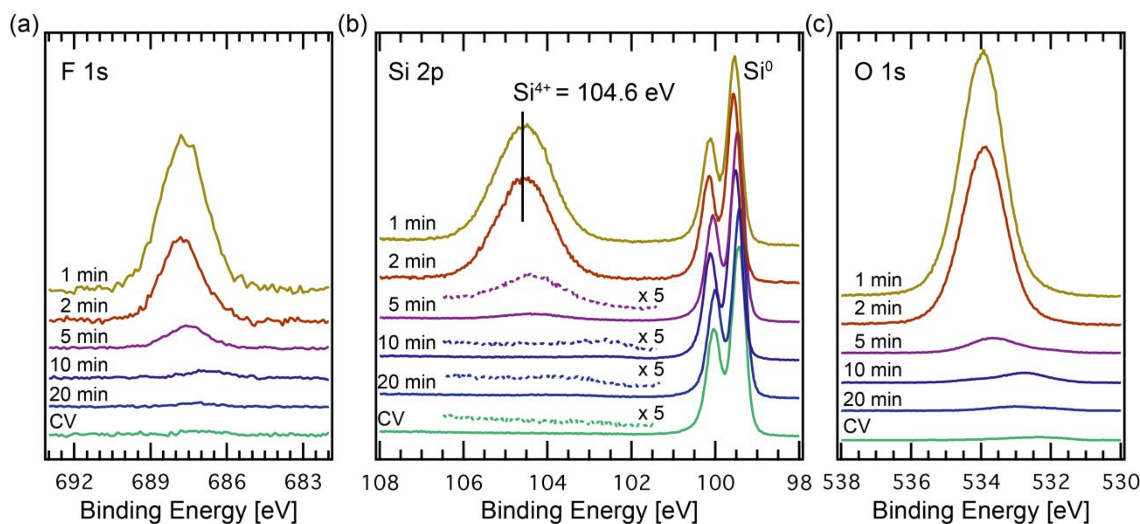

Figure 4: XPS F 1s (a), Si 2p (b), and O 1s (c) core-level spectra of n-Si(100) samples where the CA scan (at E = +6 V) was stopped at different times. The amount of Si^{4+} (b) is reduced for increased etching time. A direct correlation between the intensity of Si^{4+}, F 1s and O 1s is visible; note that Si^{4+} denotes 4-fold coordinated Si and not a partial charge of 4. The intensities are normalized to the intensity of the Si bulk line Si^0.

Figures S7a-b show the shifts in the Si^{4+} core level with potential and with time during CA. The charge passed during CA was linear with time (Figure S7c).

1
2
3
4
5
6
7
8
9
10
11
12
13
14
15
16
17
18
19
20
21
22
23
24
25
26
27
28
29
30
31
32
33
34
35
36
37
38
39
40
41
42
43
44
45
46
47
48
49
50
51
52
53
54
55
56
57
58
59
60

Deconvolution of the Si 2p core-level spectra (Figure 5a) indicated the presence of an signal that has been previously ascribed to a Si^{β} (tensile) stress component, where β denotes an energetic shift of the bulk Si 2p core-level signal (Si^0 2p). [36] [37] [38] [39] The difference in binding energy between the Si^0 2p and the Si^{β} 2p core-level lines was 0.27 ± 0.02 eV, which is lower than other characteristic binding energy shifts for silicon suboxides. [40] A peak at this binding energy has been ascribed previously to a change of silicon bond length on the surface (surface core level shift). [36] [37] [38] [39] The Si^{β} component remained detectable after almost complete removal of the silicon oxide and even in the absence of a detectable F 1s signal.

The F 1s core-level spectra showed contributions from two emissions: a strong emission at a binding energy of 687.8 eV (Figure 5b), and a peak at 688.5 eV. The peak at 688.5 eV was observed simultaneously with the signal from silicon oxide (Figure S7d). The higher-binding-energy peak can be attributed to F-Si-O species, whereas the lower-binding-energy peak is consistent with the presence of F-Si species. [34] [41] [42] [43]

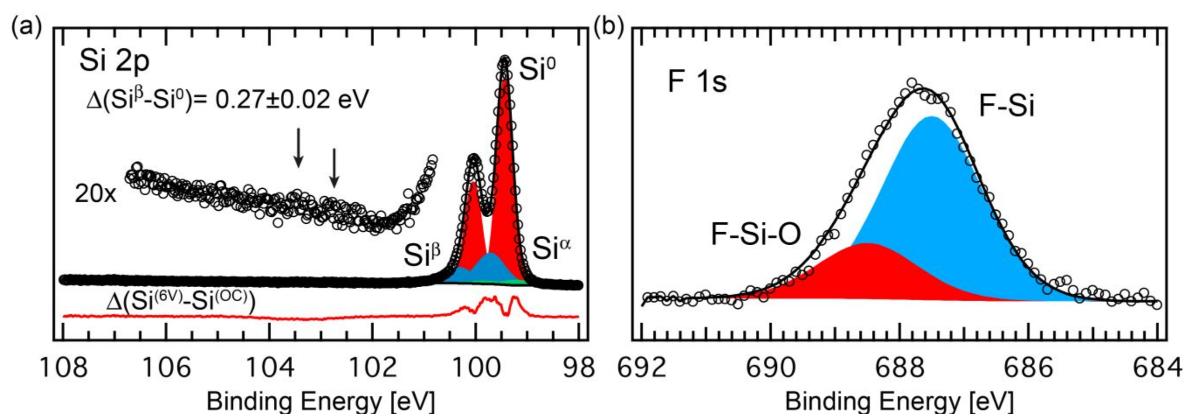

Figure 5: (a) Si 2p core-level spectra after nearly complete oxide removal at $E = +6.0$ V. No Si^{4+} component was visible; however, the main core-level line contains a tensile stress component, Si^{β}. The difference in binding energy between Si^0 and Si^{β} was 0.27 ± 0.02 eV. The arrows indicate small amounts of Si^{4+} and Si^{3+} still present. The red line below the spectra shows the difference between spectra for the sample scanned to $E = +6.0$ V and a freshly etched sample removed from the electrolyte while at open circuit. (b) F 1s core-level spectra after CA conditioning for 1 min at $E = +6.0$ V. The corresponding binding energies of the peaks are $\mathbf{E}_B$(F-Si) = 687.5 eV and $\mathbf{E}_B$(F-Si-O) = 688.5 eV.

Fractal etching near electrically isolated regions and bubbles

To gain insight into the role of bubbles in the formation of fractal-etch patterns, back-illuminated potentiostatic etching was performed on n-Si(100) samples prepared with dots of insulating epoxy on the surface. These samples were designed to electrically isolate regions of the silicon from the electrolyte, analogous to the case for a gas bubble, although with a different phase boundary. Figure 6a shows the fractal-etch pattern formed around an epoxy dot. The pattern from the back-illuminated epoxy-dot-covered surface was similar to that from gas-bubble-covered surfaces (both front and back illumination). Figure 6b shows an etch pattern formed at a boundary between an electrode and an O-ring; although this etch pattern exhibited branching, the pattern was dendritic and qualitatively different from the etch patterns observed around bubbles and epoxy dots likely due to the reduced light intensity.

Figure 6c shows fractal-etch patterns formed on n-Si(100) during a control experiment designed to examine the possible influence of light focusing by bubbles on etch patterns formed on front-illuminated samples. In this case, a sample was held potentiostatically at E = +6.0 V for 10 min while being illuminated from the back side using a photon energy (λ = 455 nm, $h\nu$ = 2.7 eV) well above the Si band gap ($\mathbf{E}_g$= 1.12 eV, corresponding to λ = 1106 nm). The absorption coefficient of Si for this wavelength ($\alpha = 3.6\times10^4$ cm^{-1}) yields an absorption length of $3\alpha = 8.3\times10^{-5}$ cm, or ~ 0.8 μm, so photogenerated holes can reach the front side only by diffusion. Moreover, only thermalized excess carriers can reach the front surface. The fractal-etch patterns were indistinguishable from the etch pattern formed around gas bubbles, and exhibited the square etching pattern typical of n-Si(100) at an early stage (Figure 3b). The less-developed pattern observed for the sample illuminated from the back with 455 nm light can be attributed to the reduced concentration of excess carriers that reach the junction with the electrolyte relative to samples back-illuminated with white light.

1
2
3
4
5
6
7
8
9
10
11
12
13
14
15
16
17
18
19
20
21
22
23
24
25
26
27
28
29
30
31
32
33
34
35
36
37
38
39
40
41
42
43
44
45
46
47
48
49
50
51
52
53
54
55
56
57
58
59
60

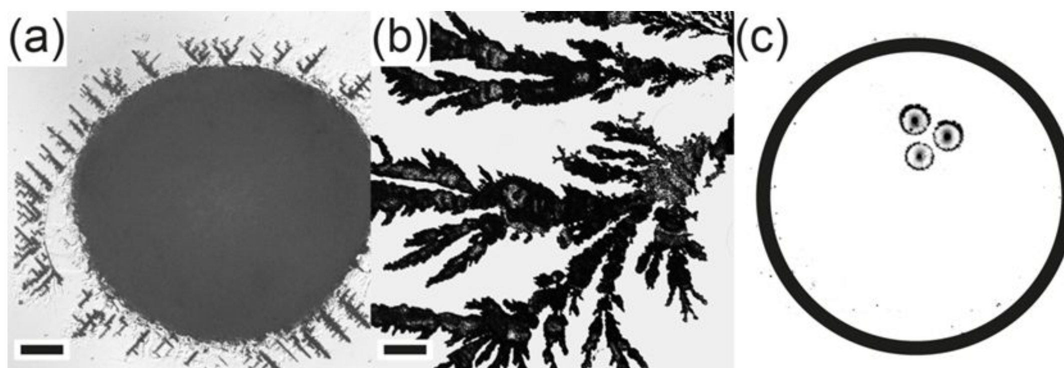

Figure 6: (a) Fractal-etch pattern formed around an epoxy dot for a back-illuminated sample. (b) Fractal-etch pattern formed near the O-ring for a front-illuminated sample (c) Image of an entire sample after etching for 10 min at E = +6.0 V in 11.9 M NH_4F(aq) under localized 455 nm back-side illumination.

Fractal dimension

Figure 7a, b shows the increase of the fractal dimension upon continued electrochemical dissolution. Over a 1 h experiment, $D_{f,2D}$ increased from 1.78 to 1.87, due to repeated branching of the quadratic base pattern. However, this branching was limited by the distance between adjacent structures. Other experimental conditions were also explored to change $D_{f,2D}$. Figure 7c shows a fractal-etch pattern obtained for a Si(111) substrate in contact with concentrated solutions of NH_4F(aq). Fractal etching on Si(111) resulted in the highest fractal dimension for Si photoelectrochemical etching observed in our work ($D_{f,2D}$ = 1.88). When photoelectrochemical etching was performed under light-limited conditions, fractal branching resulted in a shape previously observed and explained by models based on diffusion-limited aggregation theory (Figure 7d). [44]

1
2
3
4
5
6
7
8
9
10
11
12
13
14
15
16
17
18
19
20
21
22
23
24
25
26
27
28
29
30
31
32
33
34
35
36
37
38
39
40
41
42
43
44
45
46
47
48
49
50
51
52
53
54
55
56
57
58
59
60

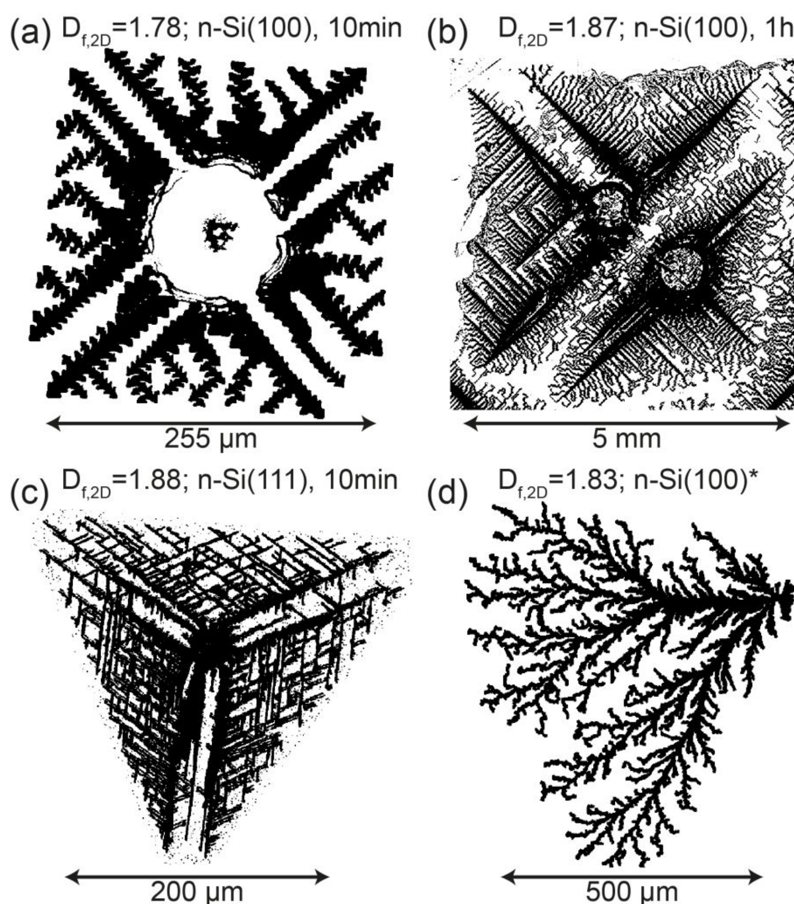

Figure 7: Fractal patterns on Si surfaces obtained upon front illumination at constant potential of $E = +6$ V and calculated fractal dimensions $D_{f,2D}$. (a) Fractal structure obtained by electrochemical dissolution for 10 min on n-Si(100), (b) corresponding structure after 1 hour, (c) fractal structure obtained by electrochemical dissolution for 10 min on n-Si(111) in 11.9 M NH_4F(aq), and (d) a structure resembling a diffusion-limited aggregation process on n-Si(100) (*: near the O-ring) after dissolution for 10 min on n-Si(111) in 11.9 M NH_4F.

Table 1 shows the values of $D_{f,2D}$ calculated for the fractals shown in Figure 3. $D_{f,2D}$ approached a value of >1.8 after 20 min of CA, due to repeated branching of the base pattern in two dimensions. Using the depth of the fractals as measured by profilometry, the three-dimensional fractal dimension ($D_{f,3D}$) was approximated as $D_{f,3D}$ ~2.5. The log(N(ε)) versus log(1/ε) plots, which results from the numerical box counting, are shown in Figure S8.

Table 1. Fractal dimension ($D_{f,2D}$) as a function of etch time for n-Si(100) samples held at $E = +6$ V vs. Ag/AgCl while illuminated from the back with 50 mW·cm^{-2} white light. The fractal-etch patterns are shown in Figure 3b-f.

Etch time (min)	$D_{f,2D}$
0	1.14
1	1.61
2	1.64
5	1.70
10	1.72
20	1.82

Surface chemistry

The mechanisms of anodic etching of Si in fluoride-containing electrolytes have been studied extensively. [4] Consequently, the focus herein is on the chemistry of the surface during fractal formation, to gain insight into the factors that determine the genesis of the observed structures.

Based on *J-E* behavior and XPS data, the formation of an anodic silicon oxide at $E < +2.7$ V led to surface core-level shifts ascribable to changes in silicon bond due to a tensile-stressed silicon surface (Si^{β}). Fractal cracking could then be facilitated by nucleophilic attack of strained bonds on the stressed Si surface. [14] [15] At potentials $E > +2.7$ V, the thin (~ 0.2 nm) anodic silicon oxide increased in thickness (~2.3 nm) upon fluoride incorporation (Figure 2 and S3), and fluoride-containing oxide also formed on the surface during CA experiments after 1 min at $E = +6.0$ V (Figure 4). These layers are denoted as having a composition of SiO_xF_y, however, the initial SiO_xF_y layers at $E > +2.75$ V may possess a different stoichiometry than SiO_xF_y layers produced at $E = +6.0$ V during the CA experiments. The ~5.0 eV difference in binding energy between the Si^0 and Si^{4+} peaks observed for samples with SiO_xF_y layers on the surface (Figure S7a,b) should, in principle, allow an estimation of the composition based on the larger electronegativity on the

Pauling scale of fluorine ($\chi = 4$) relative to oxygen ($\chi = 3.44$). [45] Although the relative intensity of the O 1s and F 1s signals can be analyzed, the transitory behavior of the oxide during electrochemical etching, and the typically amorphous character of anodic silicon oxides that contain OH groups, results in ambiguities in the analysis. Silicon oxyfluoride compounds from gas-phase experiments have been identified by photoelectron spectroscopy, [34] and the XPS binding energies observed for the SiO_xF_y layer are consistent with prior reports. [42] [43] Precipitates of $(NH_4)_2SiF_6$ also can be formed during the dissolution of SiO_2 in concentrated NH_4F. [46] However, no correlation was observed between the XPS data herein and the N 1s core-level peak, suggesting that such precipitates were not present in detectable amounts on the surfaces of our samples.

The initial circular etch patterns, related to surface bubbles, were consistently observed when SiO_xF_y was detected on the surface. Etching of the fractal structures was accompanied by a pronounced decrease of the XPS signal for oxidized Si at $\mathbf{E}_B = 104.6$ eV, indicating that under these experimental conditions, the SiO_xF_y layer was mostly removed before the fractal-etch pattern propagated with repeated branching of the base pattern. Although the decreased signal for the oxide phase that accompanied removal of the SiO_xF_y layer approached the detection limit of the XPS experiment (<0.5 ML), the Si^{β} component was still detected.

The temporal evolution of the chemical states and their intensities for O, Si and F are presented in Figure 8. Oxygen is present as surface-bound H_2O, hydroxide groups, and silicon oxide. Si-F and F-Si-O both contribute to the fluorine signal. Silicon is found in four contributions (Si, SiO_2, Si-F and F-Si-O) which are summarized in three components: Si, SiO_xF_{X-4} and SiX_yF_z. When the intensity of all species was normalized to the intensity of bulk silicon, the intensity for all species decreases with time as the fractals formed. The general trend indicates that the initially formed oxide phase was etched within the first 5 min, as evidenced by the virtual disappearance of the signals for Si^{4+}, F 1s, and O 1s. The signals reached the detection limit around 5 min, at which point the fractals started to clearly branch out from the initial bubble geometry (Figure 3d). These species coincided with the appearance of fractals (Figure S3). After the initial fast oxidation of the surface, etching of the surface became faster than further oxidation, resulting in a surface condition in which only minute amounts of O and F were present, together with water and hydroxide. The trend of the evolution of the different oxygen, silicon, and fluorine species show that these species are critical to initiate fractal etching (compare also to Figure S3). However, the

local composition could not be measured at the atomic scale to obtain information on direct exchange of F, O, and Si during etching of the branches because the signal intensity also decreased at that time. The trend of the fractal dimension had a different time constant than the evolution of F, O and Si species, and closely resembled the evolution of the branching and fractal propagation.

Previous studies of anodic photoelectrochemical etching of n-Si in diluted NH_4F (< 0.25 M) showed no formation of fractal etch patterns, but instead showed polishing of the silicon surface, [42] with a predominantly SiO_2 surface and an increase in the Si-O-F contribution at $E > 5$V as the pH decreased. Chemical etching of silicon in NH_4F produces a smooth surface which is covered with a thin layer of suboxide that can be removed by a subsequent HF etching step. [47]

During exposure to 11.9 M NH_4F with a pH of 7.2 at potentials of $E = \sim 2.75$ V, the appearance of SiO_xF_y correlated the initial formation of fractal etch patterns (Figure 1). Hence the initiation of fractal etch patterns was correlated with the presence of the tensile-stressed Si^{β} signal as well as with the appearance of SiO_xF_y on the surface. Moreover, the propagation of the pattern may depend on the continued presence and regeneration of tensile-stressed Si^{β} at the surface.

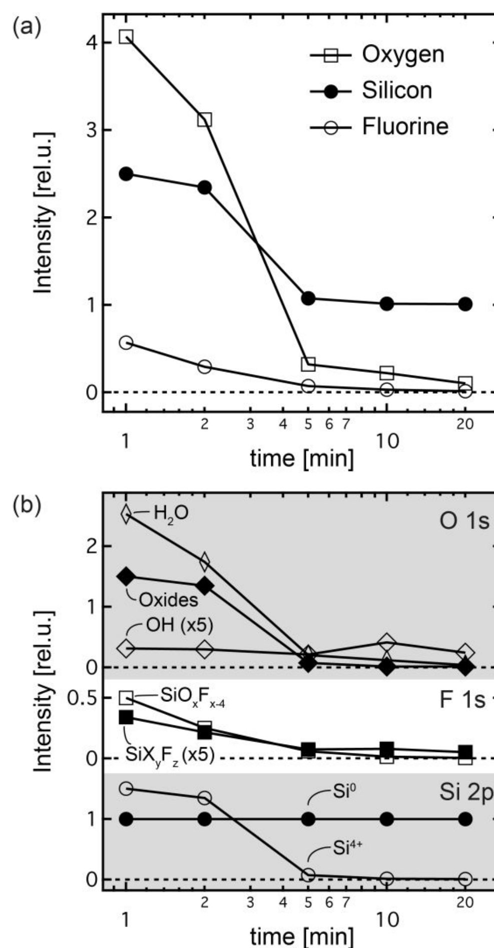

Figure 8: Evolution of the core-level intensities for the Si 2p, the O 1s and the F 1s lines from the chronoamperometric experimental data shown in Figure 4; intensities were normalized to the intensity of the Si bulk line Si^0. (a) Total normalized intensity of constituent peaks for each element, and (b) normalized intensities of each constituent peak for each element.

Initiation of fractal etching at bubble walls

The fractal-etch patterns originated at sites at which bubbles had nucleated, and propagated from points coincident with the circumferences of the bubbles. The bubbles were present on the surface of illuminated samples prior to application of a potential, and were removed at early times after the start of potentiostatic control. Hence, the bubbles that were formed at the initiation points were not necessarily present throughout the entire period of fractal genesis and propagation. Visible hydrogen evolution occurred on Si electrodes in fluoride-containing electrolytes at potentials between E_{oc} and the first anodic current peak, so the bubbles initially present on the surface are expected to be H_2 (whereas bubbles from vigorous O_2 evolution and SiF_6 formation occurred at the most positive potentials, corresponding to the plateau in the *J*-*E* data). [9]

Areas of the substrate underneath gas bubbles are not in contact with the liquid electrolyte, and are therefore electrochemically and electronically isolated. At the intersection of the bubble wall with the substrate, the phase boundary includes Si/electrolyte and Si/gas contacts. Because the Si/gas contact presents a much higher resistance to charge transfer (due to the absence of ionic species in the gas phase) than the Si/electrolyte contact, current from holes photogenerated within areas of the Si beneath the bubble will be concentrated at the Si/electrolyte/gas boundary. When a positive potential is applied to the substrate, the width of the depletion region within the Si beneath the Si/electrolyte contact will increase, increasing the penetration of the electric-field gradient into the area beneath the bubble (Figure S9). The increased penetration of the potential gradient beneath the bubble would promote the flow of light-induced holes to the three-phase boundary. [48] Hence, for as long as the bubble remains on the surface, Si oxidation should occur at a negligible rate in the electrochemically isolated area beneath the bubble, and should occur at a higher rate at the circular boundary of the bubble than on areas of the surface in contact with the electrolyte but farther from the boundary. Hence, the initial three phase boundary of Si/electrolyte and Si/gas presents a key factor for initiating fractal growth.

A plausible mechanism for fractal etching involves an in-plane stress analysis [15] in which stress is induced at the SiO_2/Si interface by the volume mismatch between Si and its oxide. Due to the volume-mismatch factor of 2.2 between Si and its oxide, a thin layer of stressed material [14] would develop more rapidly at the bubble boundary than elsewhere on the surface, and the stressed oxide [49] will be etched by the ammonium fluoride solution. The stressed silicon presents the second key component for fractal etch propagation. Etching of the oxide is expected to increase

the roughness of the surface with the formation of the fractals. The electric field would then be further enhanced near the roughness elements, increasing according to $\Delta E/r$ (where r is the radius of curvature of a pit or crevice), and would consequently produce a high concentration of photogenerated holes near the roughness elements, resulting in enhanced oxide formation, and promoting the development of three-dimensional structures perpendicular to the semiconductor-electrolyte interface. The interplay between rapid oxide formation and etching is visible by the presence of SiO_xF_y species.

The importance of electrochemical and electrical isolation of the region beneath the bubble to the initiation of fractal etching at points on the circumference is supported by the observation of fractal etching around epoxy dots (Figure 6a). Although the bubbles, and thus the electrical isolation, did not remain stationary throughout the experiment, the electrochemical and electrical isolation produced by the initial presence of a bubble could produce nanoscale roughening of areas around the circumference (Figure S10), and consequently propagation of fractal etching from those roughened areas. Although bubbles nucleated on surfaces at sites of defects, such as roughness elements or particulates, the propagation of the fractal etch patterns from many points around the circumference of a bubble, rather than from a single point in the center of the bubble, supports a mechanism in which the bubble itself, rather than the defect that led to nucleation of the bubble, acts as a driving factor for the initiation of fractal etching.

An alternative possible mechanism for the enhanced rate of etching at bubble boundaries involves optical effects of the bubbles enhancing photogeneration of holes near the bubble walls (Figure S11). However, the effects of light focusing were not the primary cause of the initial fractal formation, because both front and back illumination resulted in comparable characteristic etch pattern (Figure S5).

The initiation of fractal etching and its propagation is an interplay between various factors that balance to produce the observed structures, as opposed to random etching or directional etching that would result in polishing of the substrate. Key factors include: initial crack formation at the Si/electrolyte/gas three phase-boundary; rapid oxide growth at the boundary leading to stressed Silicon; and an increase in roughness due to etching leading to an increase in oxide growth (and stressed silicon) resulting from an electric field enhancement at rough surface elements. The formation of SiOxFy provides a signature of this oxidation-etching process.

1
2
3
4
5
6
7
8
9
10
11
12
13
14
15
16
17
18
19
20
21
22
23
24
25
26
27
28
29
30
31
32
33
34
35
36
37
38
39
40
41
42
43
44
45
46
47
48
49
50
51
52
53
54
55
56
57
58
59
60

The crystal orientation only influences the microscopic branching pattern (see Figure 7a for Si(100) and 7c for Si(111)) due the difference in surface energy and etching rate, and is not a key component of the observed behavior. The intrinsic nature of the photoelectrochemical process constrains how far branches can subdivide or propagate, and. the double layer thickness (Helmholtz layer) can provide a limitation in addition to local stress minimalization that prevents two adjacent structures from coalescing.

Previous studies on anodizing Si were mostly performed in HF electrolyte to create either highly porous silicon, deep trenches, or arrays of extremely small holes that run orthogonal to the surface.[7] [8] Expanding the parameter space to low pH dilute NH_4F electrolyte resulted in the formation of mesa-type structures which can be constructed from different crystallographic faces.[50] Dilute NH_4F was also used to electropolish silicon. [42]

Fractal dimension

The fractal dimension indicates how well a structure utilizes the space in which it resides i.e., the degree to which the self-similar structure is surface-optimized. In terms of electrolyte and charge-carrier flow, the fractal dimension can describe the tortuosity of flow (higher travel distances for higher fractal dimension), with higher values for $D_{f,2D}$ designating higher surface areas. For internal surfaces, as in storage systems, currents can be limited due to transport of electrolyte and ions to the surface. The limit in fractal branching of porous materials is given by the spatial extension of the compact Helmholtz layer and the necessity of ‘free’ electrolyte not bound to the surfaces, e.g. how many sub-branches are possible before the electrolyte layer thickness in these branches is in the order of the electrolyte double layer. This limit yields a minimum pore dimension in the range of 5 nm. In applications such as catalysis at outer surfaces, the increased fractal dimension supports higher geometrical exchange-current densities.

The observed initial fractal dimension $D_{f,2D}$ of 1.14 rapidly increased above 1.6 and saturated below 1.9. This increase may solely be related to an increase in surface coverage and filling of gaps with a minimal width of fractal branches of ~10 µm (with an internal sub µm features, Figure S10) and depth below 3 µm (typically below 1µm, see Figure S4). The minimal branch size is an intrinsic property of the specific silicon surface orientation (here (100)) and may be influenced by changing the crystal orientation (see Figure7a and 7b). An influence on the maximum obtainable fractal dimension was not observed, with both Si(100) and Si(111) substrates exhibiting a fractal dimension $D_{f,2D} \leq 1.9$ after etching.

Initiation of fractal cracking required the presence of a three-phase boundary, so standard lithographic processes may provide a pathway for directed propagation of fractal-etch structures. This approach might allow a global shape component to be added alongside the local component that depends on the Si crystal orientation. If the trenches produced by fractal etching could be sufficiently deepened with simultaneous thinning of the Si wafer, the fractal structures might find applications in Li batteries, by enabling the intercalation of high loadings of Li while reducing rates of mechanical failure due to charging cycles.

Conclusions

In situ optical observations and XPS data showed that on both front- and back-illuminated samples, fractal-etch patterns preferentially initiated and propagated around bubbles on illuminated n-Si(100) electrodes in contact with 11.9 M NH_4F(aq). Moreover the fractal dimension of the patterns increased with etching time. Electrochemical and electronic isolation of the area beneath the bubble led to enhanced rates of oxide growth and etching along the three-phase semiconductor/electrolyte/gas boundary and consistently initiated fractal etching at points on the circumference of bubbles. Similar etch patterns formed around epoxy dots deliberately placed on the surface to create electrochemically and electronically isolated regions analogous to bubbles. Chemical analysis of the surface during the fractal-etching process showed the presence of signal ascribable to a tensile-stressed silicon as well as the presence of SiO_xF_y as key components during the etch process.

ASSOCIATED CONTENT

Supporting Information

The Supporting Information is available free of charge on the ACS Publications website.

XPS core-level analysis, supporting figures and tables.

AUTHOR INFORMATION

Corresponding Authors
*E-mail: nsl@caltech.edu
*E-mail: Michael.Lublow@vdivde-it.de

ORCID
Matthias H. Richter: 0000-0003-0091-2045
Michael Lublow: 0000-0002-1586-3779
Kimberly M. Papadantonakis: 0000-0002-9900-5500
Nathan S Lewis: 0000-0001-5245-0538

Notes

The authors declare no competing financial interest.

Acknowledgements

This work was supported through the Office of Science of the U.S. Department of Energy (DOE) under award no. DE SC0004993 to the Joint Center for Artificial Photosynthesis, a DOE Energy Innovation Hub. HJL is grateful for support by DFG project Le1192-4. Research was in part carried out at the Molecular Materials Research Center of the Beckman Institute of the California Institute of Technology. Dedicated to the memory of Hans-Joachim Lewerenz.

References

1. West, G. B.; Brown, J. H.; Enquist, B. J. The Fourth Dimension of Life: Fractal Geometry and Allometric Scaling of Organisms. *Science* **1999,** *284* (5420), 1677-1679.
2. West, G. B.; Brown, J. H.; Enquist, B. J. A General Model for the Origin of Allometric Scaling Laws in Biology. *Science* **1997,** *276* (5309), 122-126.
3. Genscher, H.; Lübke, M. Electrolytic Growth and Dissolution of Oxide Layers on Silicon in Aqueous Solutions of Fluorides. *Berichte der Bunsengesellschaft für physikalische Chemie* **1988,** *92* (5), 573-577.
4. Lewerenz, H.-J.; Aggour, M. On the Origin of Photocurrent Oscillation at Si Electrodes. *J. Electroanal. Chem.* **1993,** *351* (159-168).
5. Aggour, M.; Giersig, M.; Lewerenz, H.-J. Interface Condition of N-Si (111) During Photocurrent Oscillations in NH_4F Solutions. *J. Electroanal. Chem.* **1995,** *383* (1-2), 67-74.
6. Uhlir, A. Electrolytic Shaping of Germanium and Silicon. *Bell System Technical Journal* **1956,** *35* (2), 333-347.
7. Smith, R. L.; Collins, S. D. Porous Silicon Formation Mechanisms. *J. Appl. Phys.* **1998,** *71* (8), R1-R22.
8. Lehmann, V.; Föll, H. Formation Mechanism and Properties of Electrochemically Etched Trenches in N-Type Silicon. *J. Electrochem. Soc.* **1990,** *137* (2), 653-659.
9. Zhang, X. G. *Electrochemistry of Silicon and Its Oxide;* Kluwer Academic Publishers: New York, 2001.
10. Grzanna, J.; Lewerenz, H.-J. Oscillations at the Si/Electrolyte Contact: Discretization of Phase Oscillators. *J. Phys.: Conf. Ser.* **2013,** *410,* 012160.

11. Carstensen, J.; Prange, R.; Föll, H. A Model for Current-Voltage Oscillations at the Silicon Electrode and Comparison with Experimental Results. *J. Electrochem. Soc.* **1999,** *146* (3), 1134-1140.

12. Park, B. Y.; Zaouk, R.; Wang, C.; Madou, M. J. A Case for Fractal Electrodes in Electrochemical Applications. *J. Electrochem. Soc.* **2007,** *154* (2), P1-P5.

13. Lublow, M.; Lewerenz, H.-J. Fractal Photocorrosion of Silicon Electrodes in Concentrated Ammonium Fluoride. *Electrochemical and Solid-State Letters* **2007,** *10* (8), C51-C55.

14. Lublow, M.; Bremsteller, W.; Pettenkofer, C. Lateral Distribution of Anodic Oxides and Strain on Self-Organized Fractal Silicon Photoelectrodes. *J. Electrochem. Soc.* **2012,** *159* (5), D333-D339.

15. Lublow, M.; Lewerenz, H.-J. Scaling Effects Upon Fractal Etch Pattern Formation on Silicon Photoelectrodes. *Electrochim. Acta* **2009,** *55* (2), 340-349.

16. Stumper, J.; Lewerenz, H.-J.; Pettenkofer, C. Photocurrent Doubling at Si(111): Analysis of the Surface Condition. *Electrochim. Acta* **1989,** *34* (9), 1379-1380.

17. Lewis, N. S. A Quantitative Investigation of the Open-Circuit Photovoltage at the Semiconductor/Liquid Interface. *J. Electrochem. Soc.* **1984,** *131* (11), 2496-2503.

18. Turner, D. R. Electropolishing Silicon in Hydrofluoric Acid Solutions. *J. Electrochem. Soc.* **1958,** *105* (7), 402-408.

19. Gronet, C. M.; Lewis, N. S.; Cogan, G.; Gibbons, J. N-Type Silicon Photoelectrochemistry in Methanol: Design of a 10.1% Efficient Semiconductor/Liquid Junction Solar Cell. *Proc. Natl. Acad. Sci.* **1983,** *80* (4), 1152–1156.

20. Neergaard Waltenburg, H.; Yates, J. T. Surface Chemistry of Silicon. *Chem. Rev.* **1995,** *95* (5), 1589–1673.

21. Hollinger, G.; Himpsel, F. J. Oxygen Chemisorption and Oxide Formation on Si(111) and Si(100) Surfaces. *J. Vac. Sci. Technol. A* **1983,** *1,* 640-645.

22. Stumper, J.; Lewerenz, H.-J.; Pettenkofer, C. X-Ray Photoemission Spectroscopy Analysis of Si(111) Under Photocurrent-Doubling Conditions. *Phys. Rev. B* **1990,** *41* (3), 1592–1597.

23. Cramer, L.; Duwe, H.; Jungblut, H.; Lange, P.; Lewerenz, H.-J. Interface Analysis During Etchback of Silicon Oxide. *J. Phys.-Condens. Mat.* **1991,** *3,* S77-S83.

24. Lewerenz, H.-J. Surface Scientific Aspects in Semiconductor Electrochemistry. *Chem. Soc. Rev.* **1997,** *26* (4), 239–246.

25. Zhao, K.; Wang, W. L.; Gregoire, J.; Pharr, M.; Suo, Z.; Vlassak, J. J.; Kaxiras, E. Lithium-Assisted Plastic Deformation of Silicon Electrodes in Lithium-Ion Batteries: a First-Principles Theoretical Study. *Nano Lett.* **2011,** *11* (7), 2962-2967.

26. Li, X.-Y.; Chen, L.-H.; Li, Y.; Rooke, J. C.; Wang, C.; Lu, Y.; Krief, A.; Yang, X.-Y.; Su, B.-L. Self-Generated Hierarchically Porous Titania with High Surface Area: Photocatalytic Activity Enhancement by Macrochannel Structure. *J. Colloid. Interf. Sci.* **2012,** *368* (1), 128-138.

27. Chan, C. K.; Peng, H.; Liu, G.; McIlwrath, K.; Zhang, X. F.; Huggins, R. A.; Cui, Y. High-Performance Lithium Battery Anodes Using Silicon Nanowires. *Nat. Nanotechnol.* **2007,** *3* (1), 31-35.

28. Rolison, D. R.; Long, J. W.; Lytle, J. C.; Fischer, A. E.; Rhodes, C. P.; McEvoy, T. M.; Bourg, M. E.; Lubers, A. M. Multifunctional 3D Nanoarchitectures for Energy Storage and Conversion. *Chem. Soc. Rev.* **2008,** *38* (1), 226-252.

29. Huang, Z.; Xiang, C.; Lewerenz, H.-J.; Lewis, N. S. Two Stories From the ISACS 12 Conference: Solar-Fuel Devices and Catalyst Identification. *Energ. Environ. Sci.* **2014,** *7* (4), 1207–1211.

30. Judge, J. S. A Study of the Dissolution of SiO_2 in Acidic Fluoride. *J. Electrochem. Soc.* **1971,** *118* (11), 1772-1775.

31. Hu, S.; Richter, M. H.; Lichterman, M. F.; Beardslee, J.; Mayer, T.; Brunschwig, B. S.; Lewis, N. S. Electrical, Photoelectrochemical, and Photoelectron Spectroscopic Investigation of the Interfacial Transport and Energetics of Amorphous TiO_2/Si Heterojunctions. *J. Phys. Chem. C.* **2016,** *120* (6), 3117-3129.

32. Feldman, D. P. *Chaos and Fractals: an Elementary Introduction;* Oxford University Press: Oxford, 2012.

33. Lehmann, V.; Föll, H. Minority Carrier Diffusion Length Mapping in Silicon Wafers Using a Si-Electrolyte-Contact. *J. Electrochem. Soc.* **1988,** *135* (11), 2831–2835.

34. Pereira, J.; Pichon, L. E.; Dussart, R.; Cardinaud, C.; Duluard, C. Y.; Oubensaid, E. H.; Lefaucheux, P.; Boufnichel, M.; Ranson, P. In Situ X-Ray Photoelectron Spectroscopy

Analysis of SiO_XF_Y Passivation Layer Obtained in a SF_6/O_2 Cryoetching Process. *Appl. Phys. Lett.* **2009,** *94* (7), 071501.

35. Stekolnikov, A. A.; Furthmüller, J.; Bechstedt, F. Absolute surface energies of group-IV semiconductors: Dependence on orientation and reconstruction. *Phys. Rev. B* **2002,** *65* (11), 115318.

36. Paggel, J. J.; Theis, W.; Horn, K.; Jung, C.; Hellwig, C.; Petersen, H. Correlation of Surface Core Levels and Structural Building Blocks for the Si(111)-7×7 Reconstruction Through High-Resolution Core-Level Spectroscopy. *Phys. Rev. B* **1994,** *50* (24), 18686–18689.

37. Karlsson, C. J.; Landemark, E.; Chao, Y. C.; Uhrberg, R. I. G. Atomic Origins of the Surface Components in the Si 2p Core-Level Spectra of the Si(111)7×7 Surface. *Phys. Rev. B* **1994,** *50* (8), 5767-5770.

38. Yazyev, O. V.; Pasquarello, A. Core-Level Photoelectron Spectroscopy Probing Local Strain at Silicon Surfaces and Interfaces. *AIP Conf. Proc.* **2007,** *893* (1), 7-8.

39. Yazyev, O. V.; Pasquarello, A. Origin of Fine Structure in Si 2p Photoelectron Spectra at Silicon Surfaces and Interfaces. *Phys. Rev. Lett.* **2006,** *96* (1), 157601.

40. Himpsel, F. C.; McFeely, F. R.; Taleb-Ibrahimi, A.; Yarmoff, J. A.; Hollinger, G. Microscopic Structure of the SiO_2/Si Interface. *Phys. Rev. B* **1988,** *38* (9), 6084–6096.

41. Kasi, S. R.; Liehr, M.; Cohen, S. Chemistry of Fluorine in the Oxidation of Silicon. *Appl. Phys. Lett.* **1991,** *58* (25), 2975–2977.

42. Lewerenz, H.-J.; Jungblut, H.; Rauscher, S. Surface Analysis of the Electropolishing Layer on Si(111) in Ammonium Fluoride Solution. *Electrochim. Acta* **2000,** *45* (28), 4615–4627.

43. Lewerenz, H.-J.; Aggour, M.; Murrell, C.; Kanis, M.; Hoffmann, P.; Jungblut, H.; Schmeißer, D. Interface Engineering of Photoelectrochemically Prepared Si Surfaces. *J. Non-Cryst. Solids* **2002,** *303* (1), 1-5.

44. Canessa, E.; Tanatar, B. Modeling of multibranched crosslike crack growth. *Phys. Rev. A* **1991,** *44* (6), 3471-3477.

45. Lide, D. R., Ed. *CRC Handbook of Chemistry and Physics;* CRC Press: New York, 2003.

46. Buhler, J.; Steiner, F. P.; Baltes, H. Silicon Dioxide Sacrificial Layer Etching in Surface Micromachining. *J. Micromech. Microeng.* **1997,** *7* (1), R1-R13.

47. Lublow, M.; Stempel, T.; Skorupska, K.; Muñoz, A. G.; Kanis, M.; Lewerenz, H.-J. Morphological and Chemical Optimization of Ex Situ NH_4F (40%) Conditioned Si(111)-(1×1):H. *Appl. Phys. Lett.* **2008,** *93* (6), 062112.
48. Rossi, R. C.; Lewis, N. S. Investigation of the Size-Scaling Behavior of Spatially Nonuniform Barrier Height Contacts to Semiconductor Surfaces Using Ordered Nanometer-Scale Nickel Arrays on Silicon Electrodes. *J. Phys. Chem. B* **2001,** *105* (49), 12303–12318.
49. Grzanna, J.; Notz, T.; Stempel, T.; Lewerenz, H.-J. Structure Formation at the Nanometric Scale During Current Oscillations at the Si/Electrolyte Contact. *Phys. Status Solidi (c)* **2011,** *8* (6), 1734–1738.
50. Jungblut, H.; Jakubowicz, J.; Lewerenz, H.-J. Observation of a transitory structure during porous silicon formation: Stability of Si(1×1) H-terminated surfaces and facets. *Surf. Sci.* **2005,** *597* (1), 93-101.

1 2 3 4 5 6 7 8 9 10 11 12 13 14 15 16 17 18 19 20 21 22 23 24 25 26 27 28 29 30 31 32 33 34 35 36 37 38 39 40 41 42 43 44 45 46 47 48 49 50 51 52 53 54 55 56 57 58 59 60

Table Of Contents (TOC) graphic